J Seismol (2008) 12:499–517
DOI 10.1007/s10950-008-9100-8

ORIGINAL ARTICLE

Relative source time functions of seismic events at the Rudna copper mine, Poland: estimation of inversion uncertainties

G. Kwiatek

Received: 19 October 2007 / Accepted: 13 March 2008 / Published online: 23 April 2008

Abstract The relative source time function (RSTF) inversion uncertainty assessment was performed for two small, mining-induced seismic events (M_W=2.9 and 3.0) that occurred at Rudna copper mine in Poland. The seismograms of selected events were recorded by the seismic network composed of over 60, short-period, vertical seismometers, recording ground velocity, located in the distance ranging from 400 m up to 8 km from their hypocenters. The RSTFs were calculated for each seismic station independently, using the empirical Green's function technique. The pseudospectral approximation of the sought RSTF by a finite sum of Gaussian kernel functions was used and the inverse problem was solved with the adaptive simulated annealing algorithm. Both methods improved the stability of the deconvolution procedure and physical correctness of the final solution in comparison to the classical deconvolution methods. To estimate the inversion uncertainties, classical Markov-chain Monte-Carlo techniques were used. The uncertainty analysis allows for improved selection of a priori data to the following inversion for kinematic rupture process.

G. Kwiatek (✉)
GeoForschungsZentrum Potsdam,
Telegrafenberg D427, 14473 Potsdam, Germany
e-mail: kwiatek@gfz-potsdam.de

Keywords Induced seismicity · Seismic source tomography · Monte Carlo methods · Markov chains

1 Introduction

Earthquake sources can be studied using many different techniques, depending on the number and quality of input data. In the most classical approach, spectral analysis in the frequency domain is performed (Ben-Menahem and Singh 1981), allowing for calculation of such model-free parameters as the seismic moment or corner frequency. These parameters can be used later to make the description of the earthquake source less abstract, on the basis of the assumed rupture model. Spectral analysis is a standard tool used to investigate natural and mining-induced seismic events. Another, more comprehensive method is the seismic moment tensor inversion, presented by Gilbert (1970). The linear dependence between moment tensor components and recorded amplitudes allows for relatively simple calculation of the aforementioned general parameters. Moreover, moment tensor decomposition can be performed, allowing for calculation of the dominant source mechanism (e.g., Fitch et al. 1980; Ben-Menahem and Singh 1981). The moment tensor inversion problem can be solved in either the time or the frequency domain.

Neither of the previously mentioned techniques provides enough information on the details of the rupture process; in particular, they do not reveal the spatiotemporal complexity of an earthquake source. The most comprehensive method to examine source processes is the source time function (STF) deconvolution technique, also known as seismic source tomography.

The STF describes the seismic moment release from the earthquake source, incorporating the whole spatiotemporal complexity of the process. The inversion of seismic data for the STF, called the STF tomography, provides various information on the rupture process, such as the spatial distribution of the displacement along the rupture plane, rupture velocity, and directivity effects.

STF tomography is by far not a trivial task. An insufficient amount of seismic data, its general quality, poor azimuthal coverage of seismic stations, mutual dependence of source parameters, and usually not well resolved information on the dependence of the geological medium on wave propagation are factors of crucial influence on the possible results of STF tomography (Ruff 1987; Courboulex et al. 1999; Bouchon 2003). Consequently, the final solution is usually subjected to a number of uncontrollable assumptions and factors, and thus, there is a strong need to improve both the data availability and the inversion techniques (Dębski 2004), possibly with careful uncertainty estimation of the final solution.

Various techniques have been developed to examine spatiotemporal earthquake source characteristics. One of them consists of searching first for a so-called relative source time function (RSTF) for each station independently. In the second step, the set of RSTFs is used to image the kinematic earthquake rupture process along the rupture plane.

This paper focuses on the quality improvement and uncertainty analysis of the first stage of STF tomography—namely, the RSTF inversion. This stage of inversion is vulnerable to various, often unknown factors, and we think that detailed uncertainty estimation is of crucial importance to the quality of results of the whole source tomography. The motivation for this analysis comes from the previous study on RSTF inversion (Dębski and Domański 2002) where we observed that, in one case, the resulting RSTF fulfilled the physical constraints without any explicit constraints imposed on the algorithm; however, it seems that such behaviour is not a common feature for all resulting RSTFs.

2 Methodology

2.1 Source time function

Seismic far-field radiation provides information on geological medium structure, source processes, and recording system characteristics. According to, e.g., Aki and Richards (1985), the far-field radiation $U(t, \mathbf{r})$

$$U(t, \mathbf{r}) = \int_T \int_{\mathbf{V}} G\left(t - t', \mathbf{r}, \mathbf{r}'\right) S\left(t', \mathbf{r}'\right) dt' d\mathbf{r}' \qquad (1)$$

may be represented as a convolution of Green's function $G\left(t - t', \mathbf{r}, \mathbf{r}'\right)$, describing propagation effects (including geological medium structure, site effects, and recording system response) and the STF $S\left(t', \mathbf{r}'\right)$. The integration is performed over the total rupture time T and source volume $\mathbf{V}$. STF describes the spatiotemporal history of energy release at the earthquake source, giving the most comprehensive knowledge on the rupture phenomena, such as the spatial distribution of displacements along the rupture plane, rupture velocity, or directivity effects. From a mathematical point of view, relation (1) is linear and should lead to a linear inversion procedure. However, direct estimation of STF on the basis of Eq. 1 is extremely difficult, mainly for the following reasons (Ruff 1987; Courboulex et al. 1999; Dębski 2004):

– The data (seismograms) are available only from selected points of the focal sphere and they are not uniform—the azimuthal coverage of an earthquake is frequently insufficient to perform any kind of STF tomography. Moreover, the quality of seismograms can be significantly limited by source–receiver distance and noise. Fortunately, in the case of mining-induced seismic events analyzed here, both quality and source–receiver distance are suitable for a detailed description of the rupture

process, although there is a significant problem with various near-field effects.
- The parameters that affect the shape of STF are highly correlated, and their separation is expected to be extremely difficult or even impossible to perform (Courboulex et al. 1999).
- STF should fulfil some additional, physical constraints imposed on its shape that consequently change the initial linear inverse problem into a nonlinear one (Bertero et al. 1997; Dębski and Domański 2002).
- Retrieving information on STF requires a cautious deconvolution of Green's function. It may be achieved by either theoretical (e.g., Bouchon 2003) or empirical (Hartzell 1978; Mueller 1985) estimation of Green's function, which is an additional source of uncertainties.

In conclusion, STF deconvolution is a volatile procedure, prone to various, often not very well resolved or even unknown instabilities. Thus, a detailed and exhaustive uncertainty analysis seems to be of crucial importance.

2.2 Two stages of STF inversion

The common assumption on the earthquake rupture process is that the energy release occurs mainly on the fault plane[1] (e.g., Ben-Menahem and Singh 1981; Gibowicz and Kijko 1994) and that the variations of Green's function within the earthquake source can be neglected. These two assumptions allow us to simplify Eq. 1, which can be rewritten for a given station j as:

$$U_j(t) = \int_T G_j(t-t') \underbrace{\int_\Sigma S\left(t' - \delta\left(\mathbf{r}'\right), \mathbf{r}'\right) d\mathbf{r}'}_{\overline{S}_j(t')} dt', \tag{2}$$

where Σ is the fault plane assumed a priori and $\delta\left(\mathbf{r}'\right)$ is the retardation factor dependent on rupture propagation along the fault plane. The underbraced part of Eq. 2 denotes the STF visible by a given station j, located at the distance $\mathbf{r}$ from the earthquake's source area. This important simplification allows us to split the source tomography task into a two-step procedure:

1. The inversion for RSTFs, which can be performed independently for each station:
$$\left\| U_j(t) - \int_T G_j(t-t') \overline{S}_j(t') dt' \right\| = \min. \tag{3}$$
This stage requires knowledge on the shape of Green's function.
2. The inversion for STF:
$$\sum_j^{no.\,stations} \left\| \overline{S}_j(t) - \overline{S}_j^{syn}(t) \right\| = \min, \tag{4}$$

where $\overline{S}_j^{syn}(t)$ is the synthetic $\overline{S}$ according to the chosen model. The second stage of STF tomography is not considered in our study, and we focused on the uncertainty estimation of the first stage of STF tomography.

2.3 RSTF deconvolution

The accuracy of the first stage of STF inversion is of crucial importance for the quality of the final tomographic solution of the second stage. Herein, we concentrated on the first part of source tomography, the RSTF deconvolution, believing that the proper calculation of the RSTFs with exhaustive uncertainty estimation makes the final results more reliable. As was pointed out in the previous section, retrieving information on RSTF requires estimation of Green's function. In the case of a complicated geology and high frequencies of recorded seismic waves, the empirical Green's function (EGF) method is highly recommended (Hartzell 1978; Mueller 1985). The EGF method relies on replacement of an original and unknown Green's function with part of the waveform of another seismic event, smaller by about two orders of seismic moment (e.g., Lay and Wallace 1995), which had occurred as close as possible to the investigated one. Both events should have a similar focal mechanism. Such an empirical approximation of Green's function is valid up to the corner frequency of the EGF event used in the deconvolution (Mueller 1985).

Having estimated Green's function, the RSTF deconvolution becomes a typical inverse task,

[1] This assumption removes all effects connected with the nonplanarity of the earthquake rupture process

given by Eq. 3, which can be solved either in the frequency, e.g., spectral division (SD) deconvolution (Mueller 1985), or in the time domain—e.g., projected Landweber (PL) deconvolution (Bertero et al. 1997). However, both aforementioned methods suffer from numerical instabilities and consequently require a lot of subjective interaction (Dębski and Domański 2002). Furthermore, the RSTF must fulfil additional, physical constraints such as a nonnegativity, causality, finite duration time, and frequency band (Bertero et al. 1997; Dębski and Domański 2002). The incorporation of all of these constraints into the PL or SD deconvolution methods is problematic and, as a consequence of such an inclusion, the inverse task for the first stage of the STF tomography becomes a nonlinear one.

2.4 Pseudospectral approximation of RSTF

In this paper, we used the pseudospectral (PS) approximation of RSTF. The PS technique (e.g., Fornberg 1996) was tested by Dębski and Domański (2002) in the context of STF deconvolution. The tests performed therein on synthetic and mining-induced seismic data, as well as the comparison tests between the PS and PL approach, proved the usefulness and stability of the PS deconvolution technique in the first stage of STF tomography.

The most important element of the PS method used here is the parametrization of $\overline{S}$ by a finite sum of Gaussian kernel functions:

$$\overline{S}\,(t;\mathbf{a},\mathbf{t},\boldsymbol{\sigma}) = \sum_{k=1}^{no.\,kernels} a_k \exp\left[-\frac{(t-t_k)^2}{2\sigma_k^2}\right], \qquad (5)$$

where a_k, t_k, and σ_k, elements of vectors $\mathbf{a}$, $\mathbf{t}$, and $\boldsymbol{\sigma}$, are called decomposition coefficients. Thus, in the *triple* PS approximation, $\overline{S}$ may be represented by a set of three parameters, describing the amplitudes, time shifts, and widths of the gaussian kernel functions. Pseudospectral representation of $\overline{S}$ automatically ensures the positivity constraint imposed on its shape, provided that all a_k coefficients are nonnegative. Finite RSTF duration time and causality can also be met because the Gaussian kernel functions decrease relatively fast from their centers (Dębski and Domański 2002). Moreover, the limited frequency band, controlled by the $\boldsymbol{\sigma}$ parameter, is easily taken into account thanks to the Gaussian kernel function and resulting functions, and their Fourier spectra are naturally smoothed.

The PS and EGF technique modifies the inverse task from Eq. 3 into the following minimization problem:

$$E\,(\mathbf{a},\mathbf{t},\boldsymbol{\sigma}) = \left\| U\,(t) - \overline{S}\,(t;\mathbf{a},\mathbf{t},\boldsymbol{\sigma}) * \hat{G}\,(t) \right\| = \min, \qquad (6)$$

where $\hat{G}\,(t)$ is the EGF. The task relies on finding the coefficients $[a_k]$, $[t_k]$, and $[\sigma_k]$, for which the synthetic waveform $\overline{S}\,(t,\mathbf{a},\mathbf{t},\boldsymbol{\sigma}) * \hat{G}\,(t)$ fits best to the observed one. Here, the adaptive simulated annealing (ASA, Ingber 1989) was used to solve the multidimensional problem given by Eq. 6.

2.5 Adaptive simulated annealing

The inverse problem given by Eq. 6 can be solved using any suitable optimization technique. However, one should consider that the misfit function $E\,(\mathbf{a},\mathbf{t},\boldsymbol{\sigma})$, presented in Eq. 6, is multidimensional and nonlinear because of PS parametrization variables and physical constraints imposed on the shape of RSTF.

Various optimization techniques have been developed throughout the years, including iterative linear, gradient-based, or grid search methods. In fact, the first two methods assume that the misfit function has a well-defined minimum, and they fail when it has several peaks or troughs. Moreover, these local methods will always find the minimum closest to the starting model (Sen and Stoffa 1995), and the calculated solution may be completely wrong. The third method, namely, the grid search technique, can be useful only if the number of parameters is very small because it relies on a systematic search through all possible models to find the one that has the smallest value of misfit function (Eq. 6), or corresponding maximum likelihood (Eq. 9, see Section 2.7) when the probabilistic approach is used. Pure Monte-Carlo methods, despite being robust, seem to be expensive if the only thing we need is the maximum likelihood model $\mathbf{a}^{ml}$ or the global minimum of the multidimensional misfit function.

Simulated annealing (SA) (Kirkpatrick et al. 1983) is an alternative method for searching for the global minimum of a misfit function (see Sen and Stoffa 1995, for a comprehensive review of SA algorithms). The algorithm simulates numerically the process of chemical annealing (cf. Sambridge and Mosegaard 2002) in which a melted crystalline material is cooled slowly through its freezing point. A sufficiently slow cooling of the system should result in convergence to a near-optimal configuration characterized by a near-minimal value of energy (corresponding, for example, to the misfit function). In this study, we used one of the extensions to the original SA algorithm, namely, ASA (Ingber 1989).

2.6 PS/ASA deconvolution reliability tests

The pseudospectral approximation of RSTF using Gausian kernel functions, shown in Eq. 5, is similar to that used by Dębski and Domański (2002). In this paper, we also examined a few different parametrizations (e.g. variable a_k, constant σ_k values, and fixed t_k kernel time delay shifts) still using the same general Gaussian-like kernel shape. These tests were performed on real data, mainly to check the reliability and efficiency of optimization for various RSTF parametrizations, also with comparison to the SD and PL techniques. The details of this analysis are shown in Section 4.1. As a result, the performed tests proved that the similar RSTF deconvolution quality and reliability can be gained, when the following misfit function is considered:

$$E(\mathbf{a}) = \left\| U(t) - \overline{S}(t;\mathbf{a}) * \hat{G}(t) \right\| = \min, \qquad (7)$$

i.e., where time shifts $\mathbf{t}$ and kernel function widths $\boldsymbol{\sigma}$ were assumed a priori and remained constant during the RSTF inversion. This advocates Dębski and Domański's (2002) choice of PS parametrization. From a computational point of view, the inversion of RSTF using the *single* parametrization is much faster than that presented in Eq. 6, and that is why it was used as a base for the misfit function in the RSTF uncertainty analysis and the PS/ASA deconvolution tests shown in the following section.

Additionally, we investigated the reliability of RSTF inversion using the PS/ASA approach in comparison to the SD and PL algorithms. Firstly, the complex synthetic RSTFs, composed of the three peaks of variable amplitude, were generated and then convolved with a few real EGFs from events investigated in this study (see Fig. 1). Secondly, the Gaussian noise of variable intensity has been added to the convolved trace, and the resulting waveform was subsequently used as the input seismogram for the following inversion task using the PS/ASA, SD, and PL approaches. In the case of SD inversion, the low pass 15-Hz Butterworth filter was applied to the final RSTF solution and the water level was used to stabilize the inversion procedure. The PL inversion was stopped after approximately 70 iterations (depending on analyzed case) to suppress the increasing numerical distortions. For the PS/ASA approach, the vector of time shifts $\mathbf{t}$ and kernel function widths $\boldsymbol{\sigma}$ remained constant during the RSTF inversion, and the elements of vectors were equal to $t_k = 0, 8, 16, 24, \ldots$ ms and σ_k=16 ms, respectively. As a result, the pseudospectral approximation consisted of over 60 Gaussian kernels of equal widths, fixed time shifts, and variable amplitude. The annealing scheme for ASA algorithm was adjusted empirically. The results of inversion for various signal-to-noise ratios are presented in Fig. 1.

For the high signal-to-noise ratios, the reconstructions of RSTF are reliable and similar to the assumed input model no matter what deconvolution method was used. However, for the noisier input seismograms, the SD deconvolution approach becomes more unstable, resulting in a less clear solution that frequently does not follow the physical constrains imposed on the shape of RSTF. The PL deconvolution results are, in most cases, comparable with respect to pseudospectral approach and quite insensitive to changes in signal-to-noise ratio. However, in our case, the deconvolution had to be performed semimanually because of the frequent corruption of solution by the ill-posed deconvolution in later inversion stages caused by the noisy data. It resulted sometimes in the creation of additional, artificial peaks before and after the main seismic moment release and had to be removed manually. The PS/ASA algorithm turned out to be practically insensitive to the noise

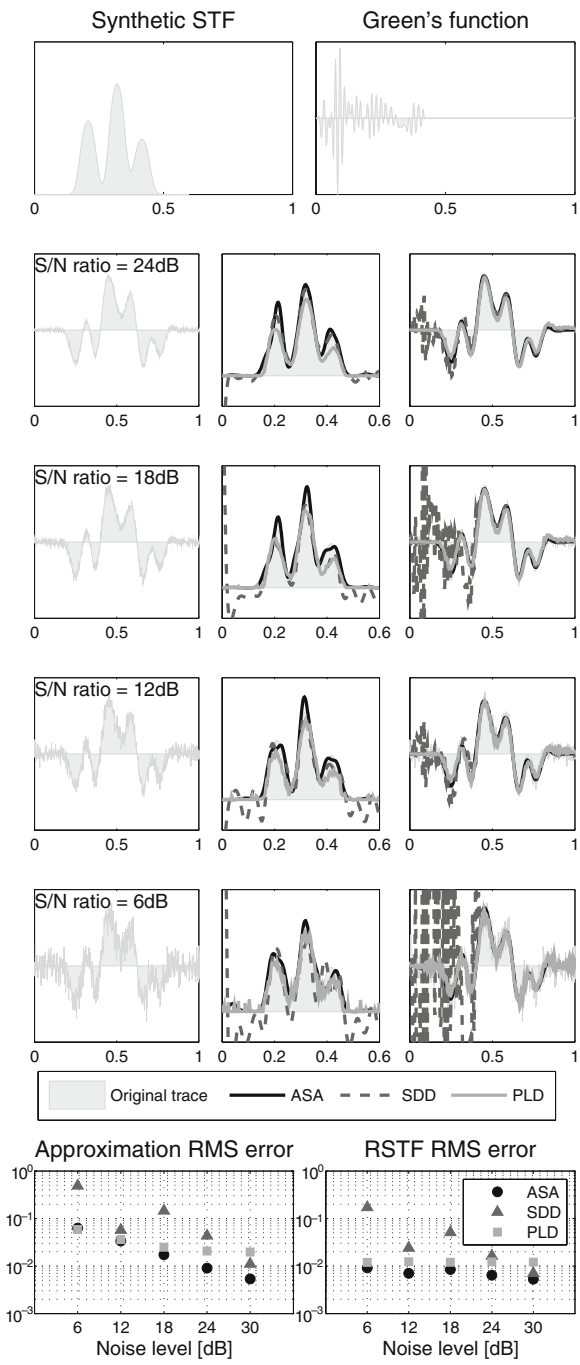

Fig. 1 The comparison of the PS/ASA, PL, and SD deconvolution efficiency using the synthetic RSTF (*top-left picture*) and real Green's function (*top-right picture*) (see text for details). The next four rows present the results of deconvolution for various signal-to-noise ratios (24, 18, 12, and 6 dB). *First column*: input seismogram (cf. different noise level). *Second column*: reconstructions of the synthetic RSTF (*shaded area*, same as in the *top-left picture*) using different deconvolution methods (PS/ASA: *solid, black line*, SD: *dashed, greyed line*, PL: *solid, greyed line*). *Third column*: comparison of fit between calculated and input synthetic seismograms for different deconvolution methods. *Horizontal axes* denote time in seconds. *Last row*: comparison of RMS errors between synthetic RSTF and RSTF reconstructions (*bottom-right picture*) and between input and calculated seismograms (*bottom-left picture*) for different signal-to-noise ratios and deconvolution methods

increase, and we obtained well constrained solutions that fulfilled the physical constrains: the causality, nonnegativity, and finite duration. The resulting RSTFs were naturally filtered during the inversion processes by the Gaussian kernels. However, a few efforts had to be made before the deconvolution to adjust the ASA cooling schedule. It is also worth mentioning that the PS/ASA approach is much slower in comparison with the remaining two algorithms.

2.7 Uncertainty estimation

The uncertainties in the RSTF inversion solution are caused by many factors, such as signal noise, discrepancy in event location or focal mechanism in EGF approach, and theoretical errors caused by approximate or simplified calculation of theoretical seismograms, to name a few. Consistent treatment of these uncertainties is possible with the probabilistic inverse theory (Tarantola 2005). The most important advantage of this technique is that it allows us to incorporate the uncertainty analysis into solving the inverse problem.

The probabilistic approach to inversion generally relies on sampling the a posteriori probability density function (PDF). According to Eq. 7, in our study, the a posteriori PDF $\sigma(\mathbf{a})$ equals the product of a priori probability densities $\sigma^{apr}(\mathbf{a})$ and the likelihood function $L(\mathbf{a}) = \exp(-E(\mathbf{a}))$:

$$\sigma(\mathbf{a}) = \sigma^{apr}(\mathbf{a})\, L(\mathbf{a}). \tag{8}$$

This distinction describes all the information we have and constitutes the complete solution to the inverse problem (Mosegaard and Tarantola 1995).

There are a few different methods to inspect the a posteriori distribution and extract the required information. Someone interested only in

searching for the best solution might want to calculate the maximum likelihood model:

$$\mathbf{a}^{ml} = \arg_{\mathbf{a}} \left[\max\left(\sigma\left(\mathbf{a}\right)\right)\right], \tag{9}$$

which maximizes the a posteriori PDF and practically reduces the probabilistic approach to the optimization technique (Dębski 2004).

Generally, whenever we search for a solution of the inverse problem other than the maximum likelihood model, we have to sample the a posteriori distribution $\sigma\left(\mathbf{a}\right)$, usually using the Monte Carlo techniques. If the number of parameters is small, $\sigma\left(\mathbf{a}\right)$ can be estimated by direct calculations over a predefined multidimensional grid or "blind" sampling. If it is large, as it is in the case of PS approximation of RSTF, the $\sigma\left(\mathbf{a}\right)$ PDF may be sampled using the Markov chain Monte Carlo (MCMC) technique (Mosegaard and Tarantola 1995).

MCMC is a strategy for generating samples from the target distribution using a Markov chain mechanism. A Markov chain is an ordered set of samples where each sample (i.e., the specific value of the $\mathbf{a}$ vector, also known as the current "state" of the chain or the chain's "link") depends only on the previous sample and not on the whole evolution history. For $\mathbf{a}$, we can recapitulate the previous sentence in the following form (see e.g., Andrieu et al. 2003):

$$\sigma\left(\mathbf{a}^{(i)}|\mathbf{a}^{(i-1)}, \ldots, \mathbf{a}^{(1)}\right) = T\left(\mathbf{a}^{(i)}|\mathbf{a}^{(i-1)}\right), \tag{10}$$

where $\mathbf{a}^{(i)}$ is the i-th sample in Markov's chain and $T\left(\cdot\right)$ is the transition probability. If additional requirements are fulfilled, such as the homogeneity, irreducibility, and aperiodicity of a chain, the samples created using the MCMC strategy, though locally correlated, will mimic samples drawn from the target distribution $\sigma\left(\cdot\right)$ no matter what starting point is chosen (see e.g., Andrieu et al. 2003). The other crucial property of MCMC is that the chain spends more of its time in the most important regions of the target PDF; thus, it is computationally much more efficient than a "blind" sampling, or sampling over a predefined grid (Sambridge and Mosegaard 2002).

The most popular MCMC method is the Metropolis–Hastings (MH) algorithm (Metropolis et al. 1953; Hastings 1970). In this study, we used a modification of MH, namely Metropolis "random walk" algorithm (MRW), depicted in Fig. 2. An MRW step involves sampling a candidate value $\mathbf{a}^{(*)}$, given the current values $\mathbf{a}^{(i-1)}$ according to a specified proposal distribution: $\rho\left(\mathbf{a}^{(*)}|\mathbf{a}^{(i-1)}\right)$. The chain then moves towards $\mathbf{a}^{(*)}$, i.e., $\mathbf{a}^{(i)} = \mathbf{a}^{(*)}$, with acceptance probability $A\left(\mathbf{a}^{(*)}, \mathbf{a}^{(i-1)}\right)$; otherwise, it remains at $\mathbf{a}^{(i-1)}$, $\mathbf{a}^{(i)} = \mathbf{a}^{(i-1)}$, and a new candidate is sampled. The proposal distribution must be chosen carefully to sample the space of decomposition coefficients well enough. Here, we chose the proposal distribution in the standard form of Gaussian PDF, $\rho\left(\mathbf{a}^{(*)}|\mathbf{a}^{(i-1)}\right) = N\left(\mathbf{a}^{(i-1)}, \gamma\right)$, and the width of the proposal distribution, γ, was adjusted automatically to keep the acceptance ratio between 40% and 60%.

The MRW algorithm performed a random walk in the space of decomposition coefficients, generating an ensemble of RSTF models from the a posteriori distribution given by Eq. 8. The misfit function (7), thus, the likelihood function, was slightly modified into the following form:

$$E\left(\mathbf{a}\right) = \left(1-\beta\right)\left\|U\left(t\right) - \hat{G}\left(t\right) * \overline{S}\left(t;\mathbf{a}\right)\right\| + \beta\left\|\mathbf{a} - \mathbf{a}^{ml}\right\|, \tag{11}$$

where $\mathbf{a}^{ml}$ is the maximum likelihood model from PS/ASA optimization and β describes the influence of a priori model on the result of RSTF deconvolution. The modification of the misfit function was caused by a different proposal distribution $\rho\left(\mathbf{a}^{(*)}|\mathbf{a}^{(i-1)}\right)$ and the lack of any constraints for samples generated by the MRW algorithm (i.e., they might be negative).

Set initial value for $\mathbf{a}^{(0)}$
For $i = 1, 2, \ldots,$ *no. samples*:
  Sample $u \sim U\left[0, 1\right]$ from uniform distribution
  Sample a candidate $\mathbf{a}^{(*)} \sim \rho\left(\mathbf{a}^{(*)}|\mathbf{a}^{(i-1)}\right)$
  If $u < A\left(\mathbf{a}^{(*)}, \mathbf{a}^{(i-1)}\right) = \min\left\{1, \frac{\sigma\left(\mathbf{a}^{(*)}\right)}{\sigma\left(\mathbf{a}^{(i-1)}\right)}\right\}$ then:
    Accept new model $\mathbf{a}^{(*)}$
    $\mathbf{a}^{(i)} = \mathbf{a}^{(*)}$
  else:
    Stay in the same place: $\mathbf{a}^{(i-1)}$
    $\mathbf{a}^{(i)} = \mathbf{a}^{(i-1)}$
End loop

Fig. 2 Pseudo-code for the MRW, a modification of the MH algorithm

The resulting ensemble of decomposition coefficients for each seismic station $\left\{\mathbf{a}^{(i)}\right\}_{i=1}^{Ni}$ served to estimate the RSTF inversion uncertainties, namely:

– Calculation of the mean RSTF model:

$$\overline{\overline{S}(t)} = \frac{1}{Ni}\sum_{i=1}^{Ni}\overline{S}\left(t;\mathbf{a}^{(i)}\right). \tag{12}$$

– Estimation of the variance of the RSTF model:

$$\sigma_{\overline{S}}^{2}(t) = \frac{1}{Ni}\sum_{i=1}^{Ni}\left(\overline{S}\left(t;\mathbf{a}^{(i)}\right) - \overline{\overline{S}(t)}\right)^{2}. \tag{13}$$

– Estimation of the marginal distribution for any decomposition coefficient.

$$\sigma_k(a_k) = \int \sigma(\mathbf{a}) \prod_{j\neq k} da_j. \tag{14}$$

3 Data

3.1 Geological background

"Rudna," "Lubin," and "Polkowice–Sieroszowice" are three currently operating Polish copper ore mines that exploit one of the world's biggest copper ore deposits. The considered mining area is located in the southern part of Poland in the Lower Silesia region, covering an area of about 468 km^2. Due to the scale of mining operations performed there and the location of copper smelters and refineries, the region is often called the Legnica–Glogow copper district (LGCD).

The extraction of copper deposits occur at a depth of 600–1,380 m.[2] The copper body, connected with Zechstein (upper permian) sediments, is part of a geological structure called the Foresudetic Monocline. The Foresudetic Monocline, composed of upper Permian and Mesozoic sediments, inclines gently in the northeast direction and is covered by tertiary and quaternary layers. The deposit is of the stratified type, and it is located within the sedimentary rocks mainly as accumulations of copper sulfides. These accumulations occur within copper shales, sandstones, and carbonaceous rocks of Zechstein. Depending on location within the LGCD region, the thickness of deposits varies from 0.2 up to 19 m (average 4.84 m). Various room-and-pillar systems of excavation are used for extraction of the copper ore deposit, depending on the mining conditions.

One of the major problems occurring during copper ore extraction is the seismic hazard caused by various dynamic symptoms of stress relief. In the LGCD mines, both stratum-type rockbursts and roof-type rockbursts exist. Continuous observations suggest that the roof-type rockbursts dominate, mainly because of strong and stiff roof rocks over the main deposit level (Kijko et al. 1982).

3.2 Seismic network

The analyzed seismic events were recorded by two independent seismic networks, operating in both the "Rudna" and "Polkowice–Sieroszowice" copper mines. The seismic network at "Rudna" mine is composed of 32 vertical Wilmore MK2 and MK3 seismometers recording ground velocity. The seismometers are located at the level of copper ore deposits, at depths ranging from 300 down to 1,000 m. The seismic network of "Polkowice–Sieroszowice" mine is also composed of 32 sensors, which are of the same type as in the previous seismic network, but at some sites, located in the shafts, three components are recorded. Unfortunately, the three-component seismometers are not very useful because of the relatively high noise level. The depth range of the seismic network varies from 400 m down to over 1,000 m. The signals are transmitted in analogue form with FM modulation by standard cables used in mining up to a central recorder located on the ground surface. Thereupon, signals are digitized with a sampling frequency equal to 500 Hz and 14-bit resolution. The whole system works in triggering mode, its dynamics are approximately 70 dB and the recording frequency band ranges from 0.5 up to 150 Hz. The surface distributions of seismometers in both mines are shown in Fig. 3.

[2]Data source: KGHM Polska Miedź webpage: http://www.kghm.pl

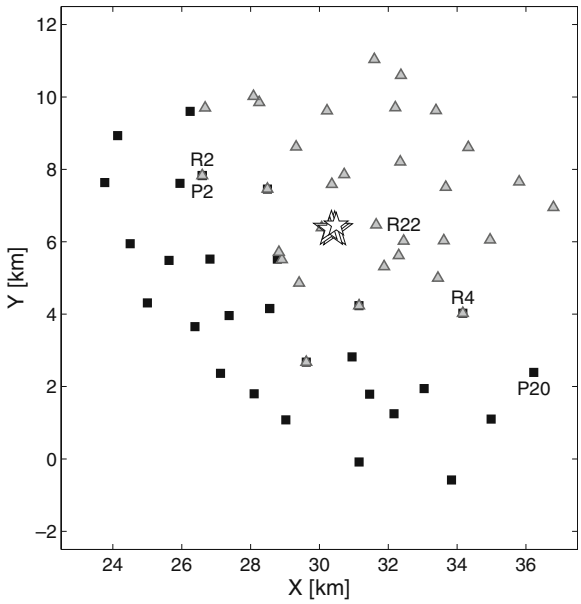

Fig. 3 The surface distribution of seismometers in a local, Cartesian coordinate system. *Triangles* denote seismometers managed by Rudna copper mine, *squares* denote those managed by Polkowice–Sieroszowice mine. The location of seismic events studied in this paper is marked with *stars*. Additional symbols: *P2*, *R2*, *R4*, *R22*, and *P20* denote seismometers used in this study to show the details of RSTF deconvolution and uncertainty analysis

Each seismic network annually records several thousand mining-induced seismic events with local magnitude M_L ranging from 0.4 up to 4.5 (Lasocki 2005), with the level of completeness of seismic catalogue equal to about 1.2. These events are considered to be directly related to the copper ore mining.

3.3 Data quality

The location of seismometers mainly at the level of copper ore deposits is disadvantageous, not only from the perspective of source tomography. One can expect seismic P waves propagating almost horizontally along the geological layers, causing problems with a proper detection of the first arrivals by the primarily vertical sensors. This results in a worse quality of event location (Kijko et al. 1982), having a simultaneous impact on the quality of seismic tomography. The errors in location might bias the quality of selection of EGFs for analyzed events which – as pointed out in Section 2.3 – must occur as close to the investigated event as possible. The similarity in location is especially important for such small events as those considered here and such small source–receiver distances. Unfortunately, the problem is augmented by the properties of the geological medium. It was proved (Kijko et al. 1982) that recorded waveforms are mainly of a refractional type, and even a small difference in an event's location can cause a substantial variation in the seismic wave travel paths and waveforms among EGFs and investigated events; thus, it can play a significant role in the quality of source tomography.

The positive characteristic of the recorded events is their predominantly good quality. This results from a high signal-to-noise ratio; close event–receiver distance, not exceeding 9,000 m; and mere influence of attenuation of seismic waves within the considered area. Additionally, a statistical analysis of the seismic catalogue proved (Orlecka-Sikora and Lasocki 2003; Kwiatek 2004) that recorded seismic events have a tendency to merge in spatiotemporal clusters, which are the reflection of mining works. The clusters simplified the selection of seismic events to the STF deconvolution using the EGF method. A few examples of recorded seismograms are shown in Fig. 4.

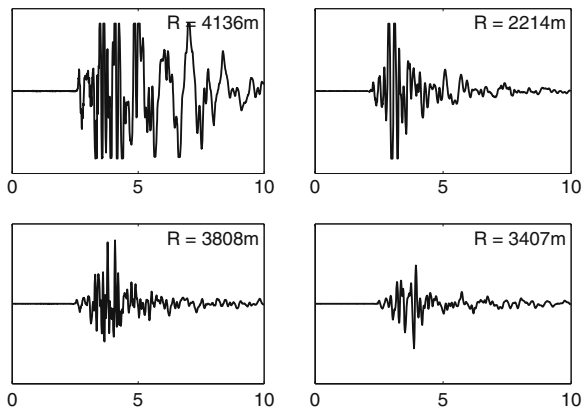

Fig. 4 A few examples of recorded seismograms. The *horizontal axis* on each seismogram denotes time in seconds. The *vertical axis* range differs for each seismogram. The distance between the seismic source and the receiver is shown in the *top-right corner* of each seismogram window

Table 1 General data for investigated events A and B and their EGFs (additional description in the text)

Event	Date	Time	X [m]	Y [m]	Z [m]	M_W	ΔM_W	ΔR [m]
A	1999-03-10	11:56	30,445	6,334	−750	3.0	0.7	146
G_1	1999-02-26	5:39	30,300	6,350	−750	2.3		
G_2	1999-04-07	5:40	30,300	6,350	−750	2.3		
B	1999-05-18	5:34	30,350	6,350	−750	2.9	0.8	182
G_3	1999-05-27	14:48	30,492	6,464	−750	2.1		

The location of events is in the local, Cartesian coordinate system. M_W is the moment magnitude, $\Delta M_W$and ΔR are differences in moment magnitude and distance between EGF and investigated event, respectively

3.4 Preprocessing

We analyzed two events that occurred in 1999 in the "Rudna" mining area. These events were thoroughly studied in other papers (Domański et al. 2002; Domański and Gibowicz 2003; Gibowicz et al. 2003) in the context of seismic source parameters, focal mechanisms, and STF deconvolution using the SD and PL methods. The general information on selected events is shown in Table 1, and their location is presented in Fig. 3. The analyzed events are of moderate moment magnitude, equal to 3.0 for event A and 2.9 for event B. Both earthquakes occurred in the middle of the seismic network, close to the boundary between "Rudna" and "Polkowice–Sieroszowice" mining areas, and, consequently, were recorded by all stations.

In the beginning, seismic moment tensor inversion in time domain was performed, based on the amplitudes of the first P-wave pulses (e.g., Fitch et al. 1980), using special software adjusted to the geological features of the LGCD (Wiejacz 1992; Domański and Gibowicz 2003). The double-couple constrained fault plane solutions were used in the further analysis, advocated by the domination of shear components (>95% of the moment tensor) in both analyzed events and EGFs chosen. The estimated fault plane parameters are shown in Table 2. Three EGF events were selected for the RSTF deconvolution procedure forming three EGF-analyzed event pairs described in this study as A/G_1, A/G_2, and B/G_3. Smaller events were selected on the basis of the following rules: difference in magnitude greater than 0.7, distance between events smaller than 200 m, and the 3D-rotation angle between the cardinal axes of double-couple solution of the pair, calculated as described in Kagan (1991), smaller than 25°.

For the following analysis, only part of the P-wave waveform from the vertical component sensors has been taken into account, from both investigated and EGF events. The S-wave phases were not used for two reasons. Firstly, they were not

Table 2 Fault plane double-couple solution parameters as a result of moment tensor inversion performed in the time domain

Event name	M_0 [$N \cdot m$]	M_0^{err} [$N \cdot m$]	Φ_A [deg]	Δ_A [deg]	Φ_B [deg]	Δ_B [deg]	Rot.angle [deg]
A	9.55×10^{12}	1.06×10^{12}	214.2	48.9	45.5	41.7	
G_1	5.16×10^{10}	6.02×10^{9}	235.1	48.1	67.0	42.5	21.0
G_2	2.43×10^{11}	2.65×10^{10}	233.8	58.7	53.2	31.3	18.9
B	2.9×10^{12}	4.52×10^{11}	260.3	46.2	70.9	44.2	
G_3	1.01×10^{10}	2.6×10^{9}	13.0	77.0	253.2	5.2	22.3

M_0 is the seismic moment calculated from the seismic moment tensor; M_0^{err} is the standard deviation of seismic moment estimation, the square root of the maximum element of the seismic moment tensor's covariance matrix; and Φ_A, Δ_A, Φ_B, and Δ_B are strikes and dips for both fault planes (in degrees). The last column denotes a 3D-rotation angle, calculated between the axes of EGF and investigated event using routines derived by Kagan (1991)

used because they were clipped in many cases and useless for the presumptive analysis. Secondly, we observed that later phases are strongly affected by the complexity of the geological medium in LGCD area (e.g., trapped waves) and probably also by local technical structures. Consequently, the wavefield in the course of S-wave arrival is complicated and not very well resolved even when only a minor change in, e.g., vertical location occurs. As a result, the inversion for S waves is usually unstable and unreliable in both analyzed events.

The last step in waveform preprocessing relied on the removement of linear trend and the application of the short, 5% von Hann's taper to both ends of extracted waveforms of EGF and investigated events.

The deconvolution was performed using both triple and single parameterization of the RSFT using the misfit functions given by Eqs. 6 and 7 to check the reliability of the PS/ASA algorithm and quality of the RSTF deconvolution while different parametrizations were used. The a priori constraints imposed on the values of $\mathbf{a}$, $\mathbf{t}$, and σ_k were as follows: the elements of $\mathbf{a}$ were assumed to be nonnegative during the inversion, $\mathbf{t}$ varied from 0 to 500 ms, the maximum expected duration of RSTF for variable $\mathbf{t}$ (triple parametrization), or $t_k = 0, 16, 32, 48, \ldots$ ms for constant $\mathbf{t}$ (single parametrization). The minimum width of kernel functions is $\sigma_k = 16$ ms and, depending on PS parametrization, remains fixed or could vary in the range of 16–40 ms. The choice of minimum kernel width came from the computation of the corner frequency of analyzed events and the corner frequency of Gaussian kernel function. The aim of such a comparison was not to lose the frequency content of recorded signals in resulting RSTFs.

The ASA algorithm searched for the global maximum of a posteriori PDF, modified by the temperature coefficient (cf. Sections 2.7 and 2.5), and the likelihood function for the triple parametrization was of the form:

$$L^{1/T}(\mathbf{a}, \mathbf{t}, \boldsymbol{\sigma}) = \exp\left(-\frac{E(\mathbf{a}, \mathbf{t}, \boldsymbol{\sigma})}{T}\right). \tag{15}$$

The a priori constraints did not allow the decomposition coefficients to be negative. The initial and final temperatures, as well as the number of iterations (equal to 50,000), were chosen on the basis of additional empirical tests. The temperature decreased in a typical ASA-like manner (see e.g., Ingber 1989), i.e., $T \sim T_0 \exp\left(-ci^{\frac{1}{\alpha}}\right)$, where α depended on the number of decomposition coefficients and c was a constant factor that was adjusted manually.

4 Results

4.1 ASA optimization

Figure 5 presents the solution of RSTF inversion for a few selected seismograms. The resulting RSTFs basically fulfil physical constraints imposed on its shape, no matter what type of parametrization has been chosen. Thanks to the Gaussian kernel functions used in PS approximation, there are no spurious, high-frequency peaks or noise. The quality of fit between the real and synthetic waveforms also seems to be very good for most of the analyzed seismograms, and it is consistent and comparable for both considered parametrization. It is worth mentioning that, in some cases, the resulting RSTFs did not completely fit the expected shape, mainly because of the absolutely improper choice of the EGF event waveform. However, in most cases, the corrections had to be applied to the selected waveforms, and then the deconvolution was repeated. These usually resulted in obtaining a more reliable solution.

4.1.1 Comparison of single and triple parametrization

To compare a single and triple parametrization in a more detailed and objective way and to determine the outlayers, we calculated two additional parameters for each analyzed pair of seismograms: the root mean squared (RMS) error between the observed and synthetic waveforms:

$$\sigma_{rms} = \sqrt{\frac{1}{T}\sum_{i=1}^{T}\left(U^{th}(t_i) - U(t_i)\right)^2}, \tag{16}$$

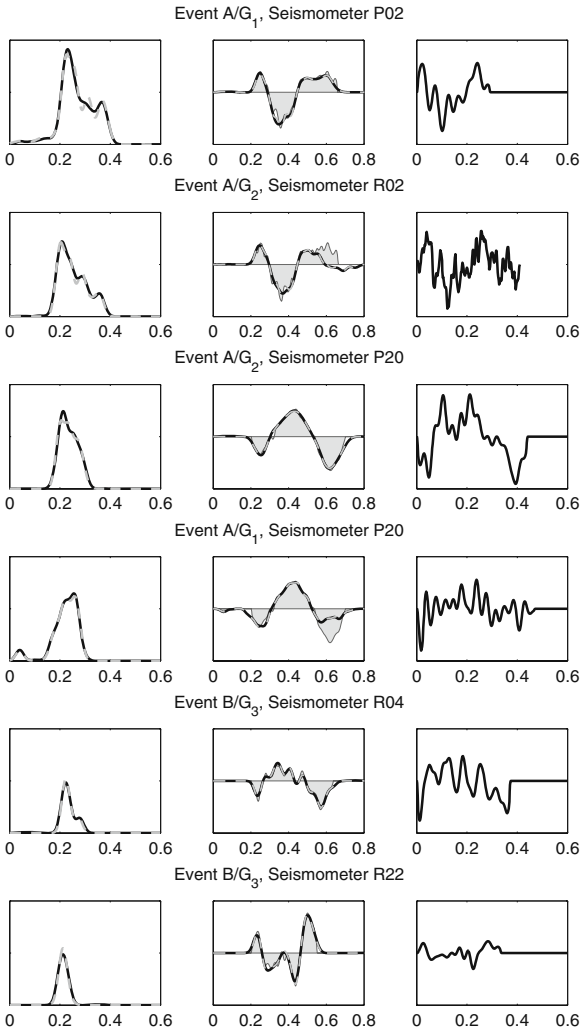

Fig. 5 Example of RSTF deconvolution results using PS/ASA approach. *Left column*: RSTF calculated using single (*solid black*) and triple (*dashed grey*) parametrization. *Middle column*: Comparison between observed (*solid greyed area*) and synthetic seismograms (*solid black* and *dashed grey lines*), obtained as a convolution of EGF (*right column*) and RSTF for single and triple parametrization, respectively

where T is the number of samples and the relative seismic moment M_0^{rel}:

$$M_0^{rel} = \int \overline{S}\,(t)\,dt, \tag{17}$$

i.e., seismic moment normalized by the moment of the EGF used in the deconvolution. Figure 6 presents a comparison between the RMS values calculated for both parametrizations. In turn, Fig. 7 shows a similar comparison for the values of the relative seismic moment. It is readily seen in Figs. 6 and 7 that the final solutions in the view of RMS and relative seismic moment

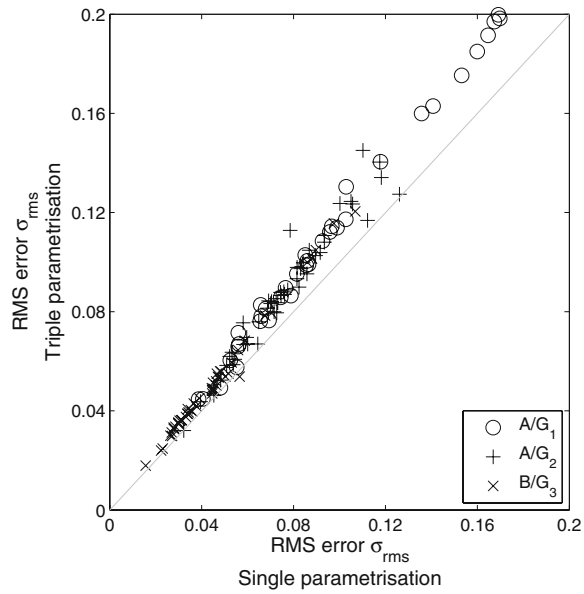

Fig. 6 Comparison of the root mean squared (*RMS*) values for single (*horizontal axis*) and triple (*vertical axis*) parametrization of the sought RSTF. Each *point* corresponds to the RMS value for a different seismogram of the same event

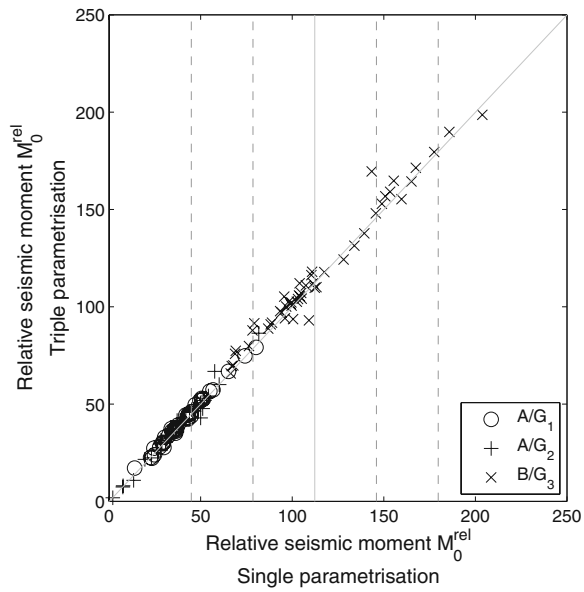

Fig. 7 Comparison of the relative seismic moments for the two different parametrizations of the sought RSTF. Each *point* corresponds to the value of relative seismic moment calculated for both parametrizations

parameters are quantitatively comparable for both single and triple parametrization; however, there exists a slight difference in RMS values—a deviation from the line of equal values is apparent in Fig. 6, which exists for both examined events. It was caused by the insufficient number of iterations performed in the ASA algorithm for the triple parametrization of the RSTF. This issue could, of course, be easily overcome, e.g., by increasing the number of iterations and decreasing the value of the final temperature, but it immediately raises the question of the usefulness of the triple parametrization. The inversion procedure then becomes definitely less efficient, with no significant change in the resulting RSTF, as is clearly illustrated in Fig. 5. The single parametrization of RSTF only requires manual adjustment of the **t** and $\boldsymbol{\sigma}$ parameters, which is relatively simple; thus, it was used in the subsequent uncertainty estimation.

4.1.2 Comparison of deconvolution methods

We also compared the results of RSTF deconvolution using a single parametrization with the solutions obtained by the SD and PL approach. We used almost the same procedure as described in Section 2.6 for the nonpseudospectral approaches, except for an additional low-pass 15-Hz Butterworth filtering in PL method that was necessary to stabilize and compare the solutions objectively. A few selected examples of calculated solutions are shown in Fig. 8 together with the results of pseudospectral deconvolution by means of the PS/ASA approach. The conclusions are similar to the ones that resulted from the synthetic tests. For the typical signal-to-noise ratio level, the quality of fit between the investigated and reconstructed waveforms remained similar for all methods (except for the significant decrease of the signal-to-noise ratio in some cases, where we have not obtained reliable SD solutions at all). This is not the case when we compare the RSTF deconvolution solutions (Fig. 8, left column). The durations of RSTF are usually consistent among different deconvolution variants, but the shapes are sometimes not. Unsurprisingly, the differences occur mostly between the unconstrained spectral and constrained PL and PS/ASA approaches, and they affect calculated source parameters (see e.g., Domański and Gibowicz 2003). Concerning the constrained solutions, there is no big difference between the RSTF obtained using any method. The most significant differences appear to be seen for some cases before and after the main seismic moment release (see, e.g., RSTF for seismometers P20 and R22) where PL solution sometimes predicts minor peaks that are not visible using the PS/ASA methodology. Usually, the pseudospectral variant of the deconvolution displays slightly smoother solutions that are consistent among different seismometers, which was of the greatest importance in the investigation of spatial and temporal changes in the seismic moment release over the predefined fault plane (cf. Kwiatek and Dębski 2006) and allowed us to calculate

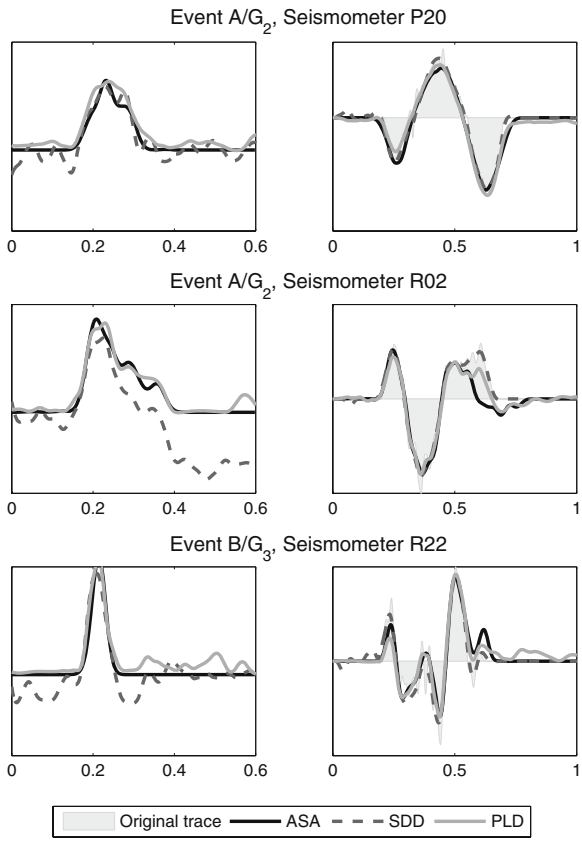

Fig. 8 The comparison of the PS/ASA, PL, and SD deconvolution efficiency using the regular seismic data from a few selected seismometers. *Left column*: Calculated RSTF deconvolution result using PS/ASA (*solid, black line*), SD (*dashed*) and PL (*solid, greyed line*) approach. *Right column*: the comparison between input and reconstructed (the convolution between EGF and RSTF) seismograms

consistent solutions that were not possible using either the PL or the SD method. Moreover, the PS/ASA approach seems to work better in the poor signal-to-noise ratio conditions, where we obtain a more reliable solution that with the PL approach. That was caused by usage of the global ASA optimizer. However, in well-defined and stable cases, where signal-to-noise ratio was high, the PL method overcame the PS/ASA approach because of the poorer time efficiency of the latter method.

4.2 Uncertainty estimation

The resulting RSTFs were used as an a priori model for the subsequent RSTF inversion uncertainty estimation. In the beginning, in the so-called burn-in stage, the width of the Gaussian proposal distribution γ (see Section 2.7) was adjusted to obtain the average acceptance ratio in the range 40–60%. After the burn-in stage, the random walk algorithm carried out 200,000 random walks in the space of decomposition coefficients, according to the Metropolis rule. The number of iterations was chosen by the trial-and-error procedure that relied on comparing the changes in resulting statistics (e.g., average RSTF model, standard deviation) when a different number of iterations was used. We have not imposed any nonnegativity constraints on the elements of **a**, as in the PS/ASA optimization. Instead, the misfit function (11) was composed of two elements: the first one described the misfit between the synthetic and real seismogram and the second one denoted the influence of the a priori model on sampled RSTFs. The a priori model was taken from the result of ASA optimization. We assumed β=5% and used the single parametrization of RSTF, where only the elements of **a** were sampled, and **t** and $\boldsymbol{\sigma}$ remained equal to their equivalents in the PS/ASA deconvolution. Finally, the resulting ensemble of decomposition coefficients, the mean RSTF model, and the standard deviation of the model were calculated, according to Eqs. 12 and 13. We also computed the PDFs for each sample of resulting waveforms.

An example of RSTF uncertainty estimation for a few selected RSTFs is shown in Fig. 9. The key features of each presented solution are shaded

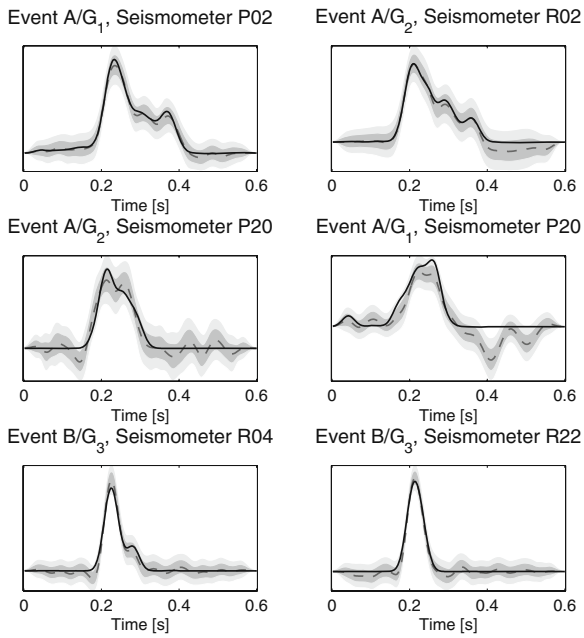

Fig. 9 Example of RSTF uncertainty estimation for six selected cases. The *black line* indicates the "best" solution calculated with PS/ASA optimization, being simultaneously an a priori model for Metropolis algorithm. The *greyed, dashed line* denotes mean solution calculated on the basis of the ensemble of RSTFs generated with Metropolis algorithm. *Greyed areas* correspond to the uncertainties in RSTF estimation—the 2σ (*light grey*) and 1σ (*dark grey*) deviations of RSTF from the mean solution (see text for a detailed explanation)

areas, denoting the uncertainties of RSTF inversion. Typically, in the PS/ASA approach or in any other optimization algorithm, only the one, "best" solution is calculated, according to the subjectively chosen misfit function and norm. However, in the Metropolis solution, each sample of the resulting RSTF waveform is represented by the corresponding PDF, not only by the sample value itself. Figure 9 compares the PS/ASA maximum likelihood solution (black line) and the mean model (dashed line). The shaded areas correspond to the 1σ and 2σ deviations of samples from the mean solution.

The resulting mean model is usually similar to the initial a priori model, especially for seismometer P02, despite the lack of nonnegativity constraints imposed on the elements of the decomposition coefficients vector. Moreover, for most of the RSTF uncertainty estimations, negative samples occur relatively rarely, which

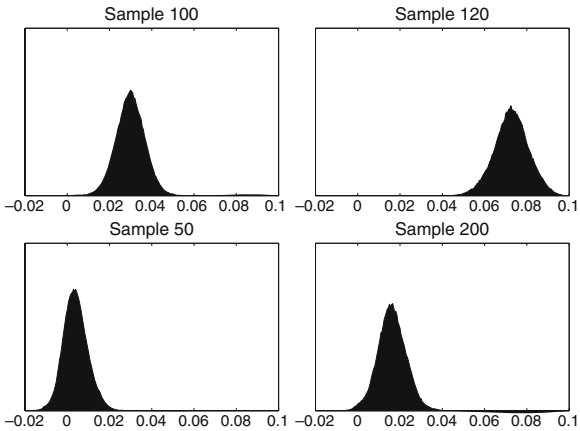

Fig. 10 Examples of the PDFs for sample numbers 50 ($T = 100$ ms), 100 ($T = 200$ ms), 120 ($T = 240$ ms), and 200 ($T = 400$ ms), calculated with the Metropolis algorithm, event A/G_2, seismometer P02

suggests that the positivity constraints have been forced mostly by the data themselves. However, it is not the case for the certain number of solutions from difference seismometers, where before and after the main seismic moment release, negative values of RSTF waveform may exist. In the case of seismometer P20 for event A/G_1, the absolute mean RSTF solution even exceeds the two standard deviations, suggesting a completely nonphysical solution. Such disturbances or oscillations were caused primarily by an improper choice of EGF waveform or the influence of some additional, unknown factors as mentioned in Section 2.6. In some cases, it was possible to correct the selections and acquire more reliable solutions. These proved the usefulness of the uncertainty estimation.

It is noteworthy that the resulting PDFs are of unimodal type, which advocates the use of standard deviation as the measure of inversion uncertainties. The widths of the PDFs vary slightly along the calculated waveforms. Four examples of PDFs for sample numbers 50 ($T = 100$ ms), 100 ($T = 200$ ms), 120 ($T = 240$ ms), and 200 ($T = 400$ ms) for seismometer P02 and case A/G_1 are shown in Fig. 10, and the 3D view of PDFs for all samples is presented in Fig. 11. The mean RSTF model mostly oscillates near the zero value,

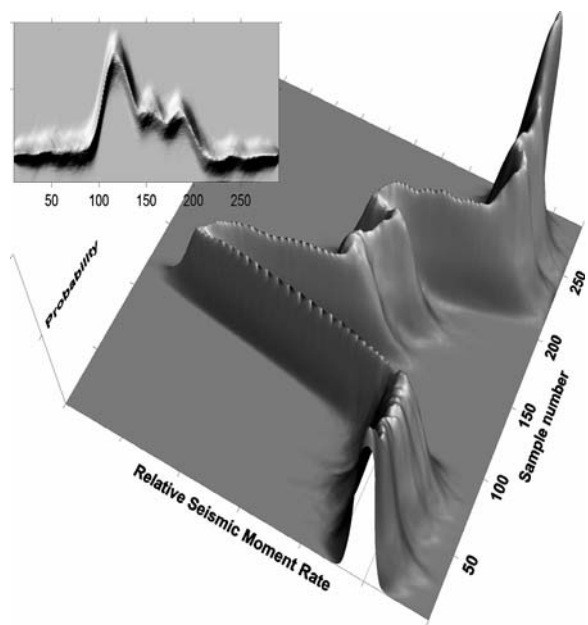

Fig. 11 The example RSTF uncertainty estimation using the MCMC random walk algorithm, applied to event A/G_1, seismometer P02 (compare with Fig. 9). The "mountain range" was created by putting the PDFs of consecutive samples side-by-side. *Picture* in the top-left corner is a view from the top. The steeper slopes reflect narrower PDFs and, therefore, smaller uncertainties. The ridge of the mountain range reflects the maximum likelihood solution, which is almost equal to the mean RSTF solution (see text for additional explanation)

which again justifies the independence of the final solution from the a priori model. In places where a strong gradient of RSTF function exists, the uncertainties usually decrease in most analyzed cases. This suggests the general shape (the rise and fall of RSTF waveform, RSTF duration) to be sufficiently well estimated.

In turn, the oscillating disturbances of RSTF waveform prior to or later than the main moment release are, for some analyzed cases, characterized by wider PDF functions. This was usually a result of the improper selection of input waveforms to the RSTF deconvolution. An interesting feature is visible in the case of seismometer P20, where the optimization result consist of only one peak (possibly characterized by the smallest value of the misfit function), whereas for the mean model carried out with the Metropolis algorithm, two equivalent peaks exist. It seems that, in this case, it is virtually impossible to check whether the moment release was accumulated in one or two peaks because the calculated uncertainty areas are relatively large and inferring such precise, high-frequency information on seismic moment release is not possible with the chosen EGF event.

To conclude, the Metropolis algorithm provided clear evidence of all limitations of RSTF inversion. One should keep in mind that the apparent complexity of the RSTFs might sometimes be just a result of wrong selection of waveforms for RSTF inversion or wrong parametrization of the RSTF (e.g., too small width of the kernel function in the PS parametrization or insufficient low-pass filtering of the resulting waveforms in the PL method). Using the MCMC uncertainty analysis, the unreliable solutions can be easily identified, which is not the case for the classical SD and PL deconvolution methods.

5 Interpretation

From Fig. 7, a slight dispersion (for almost all cases not exceeding two standard deviations from the mean value of M_0^{rel}) of the relative seismic moment M_0^{rel} is clearly seen in each analyzed case, which, in the perfect case, should be equal for all calculated RSTFs. It seems that this dispersion was caused neither by the PS parametrization nor by the ASA inversion algorithm itself because there were no significant differences in RSTFs calculated with different parametrization. The dispersion is also seen when PL and SD algorithm are used. The values of M_0^{rel} are more dispersed at closer hypocentral distances for events A/G_1 and A/G_2, which suggests the breakdown of EGF assumptions for seismometers located in the vicinity of the earthquake source. For all investigated events, a slight growth of RMS values with the distance is also seen, but the increase of noise (and, thus, problems with waveform selection) might only be a tentative explanation for this phenomenon. Generally, the stablest results come from the seismometers located at distances ranging from 3 to 5 km from the source. Such "stable" behaviour seems to be partially explained by our knowledge on the propagation of seismic waves in the LGCD area. For distances greater than about 3.5 km, the head wave refracted from the crystalline basement dominates in the recorded wavefield because the remaining direct wave and other refractional waves are relatively highly attenuated or they travel with a smaller velocity. Therefore, observed waveforms for both EGF and analyzed events are simpler, the near-field effects are significantly suppressed, and possible errors in the vertical location of seismic events play a less important role in the final shape of waveforms taken for analysis.

Calculated RSTFs differed in both analyzed cases. The duration of seismic moment release varied between 150–200 and 50–70 ms for events A and B, respectively. The study of variation of pulse width with station azimuth suggested that event A displayed a quite strong directivity effect (for additional information, see Domański and Gibowicz 2003). Assuming a unilaterally propagating rupture model, they found rupture velocity equal to 0.30 of shear velocity. However, the seismic moment release for event A seems to be even more complex than the unilaterally propagating rupture. The resulting RSTFs are frequently composed of a few bumps (cf. Fig. 5), as it is in the case of seismometers P02 and others, no matter what EGF has been used. The complexity is supported by the results of uncertainty analysis

(Fig. 9) where, in the case of seismometer R02 or P02, the resulting RSTF is clearly composed of two parts with a greater and smaller value of the seismic moment release. This encouraged us to study the rupture process of event A. We used our data to calculate the spatial distribution of displacement over the assumed fault plane (Kwiatek and Dębski 2006) and confirmed that this event displays a spatially nonuniform seismic moment release concentrated in two separate patches.

It is worth mentioning that the quality of fit between the theoretical and synthetic seismograms is generally worse when Green's function G_1 is used. This is clearly seen in Fig. 5 for seismometer P20 when one compares the results of RSTF deconvolution using different EGFs. The reason for this is not very clear; however, this discrepancy may be caused by errors in G_1 focal parameter or event location estimation.

The complexity is not a case for event B. Here, we did not observe a consistent dependence of pulse width on station azimuth. Almost all computed RSTFs are of unimodal type, with a few exceptions, where an additional minor peak followed the main seismic moment release, as it is in the case of seismometer R04 in Fig. 9. Because these distortions are not related to the angle of observation in a regular manner, it seems they were caused by the shortcomings of the EGF method.

6 Conclusions

This paper presents an example of the application of Monte-Carlo methods in uncertainty estimation, applied to the RSTF deconvolution. Knowledge on the quality of the RSTF inversion not only plays an important role in possible further assessment of total STF inversion uncertainties, but it can also improve the selection of the initial waveform data, which could simultaneously increase the homogeneity of the final solution of the seismic source tomography.

Our study was carried out on the basis of the two small mining-induced seismic events that occurred in the Polish copper ore mine. The quality and uniqueness of seismic data allowed for a detailed analysis of relatively small earthquakes, recorded by a relatively large number of seismometers, located mostly very close to the earthquake foci. These advantages simplified the selection of EGFs for the RSTF deconvolution. The only drawback of the seismic data was the inconvenient spatial distribution of seismometers, which caused an increase in the uncertainty of location of the analyzed seismic events and the fault plane solutions.

RSTF deconvolution is a nonlinear inverse task because of physical constraints imposed on the expected character of the seismic moment release in the source area. Though the inclusion of such physical constraints is relatively simple and may be performed in many ways, standard RSTF deconvolution methods, such as PL or SD deconvolution, suffer from various numerical instabilities. To suppress them, we used a pseudospectral approach to the RSTF parametrization combined with the global optimization algorithm. The pseudospectral method relied on the replacement of the RSTF by a finite sum of Gaussian kernel functions. Such parametrization enabled automatic inclusion of physical constraints imposed on the shape of RSTF. The inverse problem was solved using the ASA algorithm to assure better convergence of the misfit function to the global minimum. Additional tests were performed on both synthetic and mining-induced data to compare the developed PS/ASA algorithm with other deconvolution methods. These tests showed that combined PS/ASA deconvolution overcomes the remaining two methods in a poor signal-to-noise ratio environment.

The methodology was applied to both investigated events. The combined PS/ASA approach turned out to be a stable and reliable procedure. The calculated RSTFs clearly fulfilled all physical constraints imposed on their shape and might be used directly in the following inversion for spatial and temporal distribution of seismic moment release. We studied and compared two different parametrizations of RSTF to check whether the particular solution was not dependent on the assumed deconvolution model. We also compared the solutions with those obtained using PL and SD approaches.

Both qualitative and quantitative analysis of the estimated RSTFs showed the variation of relative seismic moment values and the general shape of the RSTF. Because calculated RSTFs depended neither on the parametrization nor on the deconvolution method, it was probably the breakdown of the concept of the EGF method that was responsible for the dispersion of the aforementioned features of RSTFs. We think that each discrepancy in the RSTF deconvolution results (which is, of course, not related to the seismic source) can start playing a more significant role in increasing the inversion uncertainties in the source tomography problem.

To estimate the RSTF deconvolution uncertainties, we used a classical Metropolis algorithm. As a result, we obtained an additional ensemble of PDFs, related to each sample of the RSTF waveform. These PDFs allowed for the calculation of two estimators: the mean and the standard deviation of the RSTF solution.

The uncertainty analysis allowed for extended discrimination in the inversion quality between different stations. It was also useful in verifying the PS parametrization—to check whether the complexity of the calculated RSTFs was only an artificial effect or, rather, a reliable signature of the complex physical processes in the source of an earthquake. These calculations were useful especially in improving the quality of the solutions and subsequent selection of RSTSs for recovering the spatial and temporal distribution of seismic moment release over the assumed fault plane.

Acknowledgements I would like to thank Professor S. Gibowicz and Dr W. Dębski for fruitful discussions and comments. I am grateful to the staff of the "Rudna," "Lubin," and "Polkowice–Sieroszowice" copper mines, particularly to Dr. M. Król and M. Burdzy, for a great deal of valuable information. This paper was partially supported by the NATO Collaborative Linkage Grant No. EST-CLG-979849 and the Polish Committee for Scientific Research Grant No. 2P04D 033 30.

References

Aki K, Richards PG (1985) Quantitative seismology. Freeman, San Francisco

Andrieu C, DeFreitas JFG, Doucet A, Jordan MI (2003) An introduction to Markov chain Monte Carlo for machine learning. Mach Learn 50(1):5–43

Ben-Menahem A, Singh SJ (1981) Seismic waves and sources. Springer, Berlin Heidelberg New York

Bertero M, Bindi D, Boccacci P, Cattaneo M, Eva C, Lanza V (1997) Application of the projected Landweber method to the estimation of the source time function in seismology. Inverse Probl 13:465–486

Bouchon M (2003) A review of the discrete wavenumber method. Pure Appl Geophys 160(3–4):445–465

Courboulex F, Deichmann N, Gariel JC (1999) Rupture complexity of a moderate intraplate earthquake in the Alps: the 1996 M5 Epagny-Annecy earthquake. Geophys J Int 139:152–160

Dębski W (2004) Application of Monte Carlo techniques for solving selected seismological inverse problems. Publ Inst Geophys Pol Acad Sci B-34(367):1–207

Dębski W, Domański B (2002) An application of the pseudo-spectral technique to retrieving source time function. Acta Geophys Pol 50(2):207–221

Domański B, Gibowicz SJ (2003) The accuracy of source parameters estimated from source time function of seismic events at Rudna copper mine in Poland. Acta Geophys Pol 51(4):347–367

Domański B, Gibowicz SJ, Wiejacz P (2002) Source time function of seismic events at Rudna copper mine, Poland. Pure Appl Geophys 159:131–144

Fitch TJ, McCowan DW, Shields MW (1980) Estimation of seismic moment tensor from teleseismic body wave data with application to intraplate and mantle earthquakes. J Geophys Res 85:3817–3828

Fornberg B (1996) A practical guide to pseudospectral methods. Cambridge University Press, New York

Gibowicz SJ, Kijko A (1994) An introduction to mining seismology. Academic, San Diego

Gibowicz SJ, Domański B, Nita B, Wiejacz P (2003) Source time function of seismic events at polish coal mines derived by Empirical Green's function approach. Acta Geophys Pol 51(1):1–22

Gilbert F (1970) Excitation of the normal modes of the earth by earthquake sources. Geophys J R Astron Soc 22:223–226

Hartzell SH (1978) Earthquake aftershocks as Green's functions. Geophys Res Lett 5:1–5

Hastings WK (1970) Monte Carlo sampling methods using Markov chains and their applications. Biometrica 57(1):97–109

Ingber L (1989) Very fast simulated re-annealing. Math Comput Model 12(8):967–973

Kagan YY (1991) 3-D rotation of double–couple earthquake sources. Geophys J Int 106:709–716

Kijko A, Dessokey MM, Gşowacka E, Kazimierczyk M (1982) Periodicity of strong mining tremors in the Lubin copper mine. Acta Geophys Pol 30:221–230

Kirkpatrick S, Gelatt CD, Vecchi MP (1983) Optimization by simulated annealing. Science 220:671–680

Kwiatek G (2004) A search for sequences of mining–induced seismic events at the Rudna copper mine in Poland. Acta Geophys Pol 52(2):155–171

Kwiatek G, Dębski W (2006) Source tomography of mining–induced seismic events at Rudna copper mine. In: First European conference on earthquake engineering and seismology, Geneva, 3–8 September

2006. http://www.igf.edu.pl/~gregus/download/posters/PKwiatek2006.pdf

Lasocki S (2005) Probabilistic analysis of seismic hazard posed by mining induced events. In: Potvin Y, Hudyma M (eds) Proc. 6th int. symp. on rockburst in mines "controling seismic risk". ACG, Chelmsford, pp 555–560

Lay T, Wallace TC (1995) Modern global seismology. Academic, San Diego

Metropolis N, Rosenbluth A, Rosenbluth M, Teller A, Teller E (1953) Equation of state calculations by fast computing machines. J Chem Phys 21:1087–1092

Mosegaard K, Tarantola A (1995) Monte Carlo sampling of solutions to inverse problems. J Geophys Res 100:12431–12447

Mueller CS (1985) Source pulse enhancement by deconvolution of an empirical green's function. Geophys Res Lett 12(1):33–36

Orlecka-Sikora B, Lasocki S (2003) Clustered structure of seismicity from the Legnica–Gşogów copper district. Publ Inst Geophys Pol Acad Sci M-24(340):104–119

Ruff LJ (1987) Tomographic imaging of seismic sources. In: Nolet G (ed) Seismic tomography. Reidel, Dordrecht, pp 339–366

Sambridge M, Mosegaard K (2002) Monte Carlo methods in geophysical inverse problems. Rev Geophys 40(3):3.1–3.29

Sen M, Stoffa PL (1995) Global optimization methods in geophysical inversion, advances in exploration geophysics, vol 4. Elsevier, Amsterdam

Tarantola A (2005) Inverse problem theory: methods for data fitting and model parameter estimation. Society for Industrial and Applied Mathematics, Philadelphia

Wiejacz P (1992) Calculation of seismic moment tensor for mine tremors from the Legnica–Glogów Copper Basin. Acta Geophys Pol 40:103–122